Nonlinear multimode buckling dynamics examined with semiflexible paramagnetic filaments

Jingjing Zhao, Di Du, and Sibani Lisa Biswal

Phys. Rev. E **98**, 012602 — Published 9 July 2018

DOI: 10.1103/PhysRevE.98.012602

Nonlinear multimode buckling dynamics examined with semiflexible paramagnetic filaments

Jingjing Zhao, Di Du and Sibani Lisa Biswal

Department of Chemical & Biomolecular Engineering

Rice University, Houston, TX, USA

We present the contractile buckling dynamics of superparamagnetic filaments using experimental, theoretical and simulation approaches. Under the influence of an orthogonal magnetic field, flexible magnetic filaments exhibit higher-order buckling dynamics that can be identified into three stages: initiation, development, and decay. Unlike initiation and decay stages where the balance between magnetic interactions and elastic forces are dominant, in the development stage, the influence of hydrodynamic drag results in transient buckling dynamics that are nonlinear along the filament contour. The inhomogeneous temporal evolution of the buckling wavelength is analyzed and the contractions under various conditions are compared.

I. INTRODUCTION

The buckling dynamics of microscopic elastic filaments are essential in numerous mechanical, biological and rheological processes. In particular, cytofilaments buckle against compressional forces to maintain the integrity of cells [1,2]; microorganisms propel themselves with the beating of the internally driven cilia and flagella [3,4]; shearing a suspension of microscopic fibers can induce fiber buckling, resulting in a non-Newtonian bulk behavior [5,6]. In comparison with the classic Euler buckling instability [7] of a compressed rigid column buckling out sideways, the buckling of microscopic elastic filaments exhibits much richer dynamics, not only because of the more flexible nature of the filaments and the addition of thermal fluctuations, but also due to the various forces to induce buckling [8–11]. Apart from studying the behavior of natural filaments, there is also a growing need to develop artificial filaments and control their movement. Paramagnetic colloidal filaments are one popular kind of such smart materials showing notable promise for spontaneous micromanipulations [12]. These artificial filaments have become analogues to natural filaments, such as flagella and cilia [13,14]. They also show great potential as micro-robots for mixing [15] as well as cargo capture and transport [16].

Buckling plays a very important role in the induced dynamics of magnetically driven colloidal filaments. Related with many complex lateral deformations, shape instabilities can be observed in various fields, such as rotational [17], precessing [18,19], oscillating [13,20], and other complex 3D magnetic fields [16]. First analytically studied by Goubault *et al.* [21], buckling dynamics of paramagnetic filaments is induced using an orthogonal magnetic field. Starting from a relatively straight linear shape, filaments undergo contractile buckling and deform into long-lasting hairpins, S-shapes and multi-folded shapes due to the balancing of magnetic and elastic forces [20,22,23]. These metastable conformations can be utilized to probe the rigidity of absorbing or grafted polymer linkers under different environments [21,24] based on the bending curvatures. Reversible buckling with long-lasting higher mode shapes was also observed in elastic media [25]. Different from classic Euler buckling, where only the first few Euler modes are considered, the onset of magnetoelastic buckling instability usually features much higher buckling modes [20,23]. This leads to a much richer dynamical behavior of the buckling mode coarsening, or mathematically, there are higher-order bifurcations after the first critical bifurcation points.

Most work to date has focused on static metastable shapes; however, the dynamics of buckling and the evolution of the pathways that a chain can take has not been well characterized. Here we explore the evolution of the contractile buckling dynamics in aqueous media. We identify three stages of the dynamics: initiation of the buckling instability, development of buckling modes and the filament reorientation and decay of these modes. With experimental, theoretical as well as numerical approaches, we analyze the inhomogeneous coarsening of the buckling curves from the onset of the buckling instability to quasi-stable multi-folded shapes.

II. MATERIALS AND EXPERIMENTAL METHODS

A. Filament sample preparation

The semiflexible filaments are fabricated using superparamagnetic colloidal particles linked together with double stranded DNA (dsDNA). The particles are streptavidin functionalized polystyrene spheres (Dynabeads® MyOne™ Streptavidin C1, Life Technologies Corp.). The mean diameter of the particles is $2a = 1.05 \pm 0.1$ μm, density is 1.8 g/cm^3, and effective volumetric magnetic susceptibility is $\chi_{eff} = 1.38$, as provided by the manufacturer [26]. DNA fragments of 1250, 2000 and 4000 base pairs (bp) are biotinylated on the 5' ends. They are formed by lysing lambda-phage DNA (New England Biolabs, Ipswich, MA) using standard polymerase chain reaction (PCR) procedures [27]. The superparamagnetic filaments are prepared inside glass chambers filled with aqueous solution (10 mM phosphate buffer solution) using methods previously described [27]. The colloidal particles are denser than the aqueous media and rapidly sediment to the bottom of the sample chamber; therefore, the filaments exist in a quasi-two-dimensional environment. Filament flexibility is able to be tuned by altering the length of DNA linkers (changing the length of springs) or adjusting the field strength for linking (changing interparticle distance).

B. Experiment set-up and imaging acquisition

The alignment, $\boldsymbol{B}_{\text{align}}$, and buckling, $\boldsymbol{B}_{\text{buckle,}}$ magnetic fields are induced using a custom-built electromagnet microscopy system. As shown in Fig. 1(a), two air-core solenoid pairs (Sargent Welch) are placed perpendicular to each other, connected to a DC power supply (HY5020E, Mastech) to create two orthogonal magnetic fields, respectively. The sample chamber is placed at the center of the two pairs of solenoids. Images of the colloidal filament system are observed using a CCD camera (Orca-HR, Hamamatsu Inc., Sewickley, PA) attached to an inverted microscope with a 20X/0.75 (air) or a 100X/1.25 (oil) Olympus objective. The strength of the applied magnetic field is measured using a Gaussmeter (AlphaLab, Inc., Salt Lake City, UT) and the direction of the applied magnetic field is determined using a paramagnetic filament of particles. The solenoid pairs are aligned to ensure that the filament was 90 degrees relative to the orthogonal solenoid pair. The alignment magnetic field is removed while the buckling magnetic field is applied simultaneously causing the filaments to buckle, as depicted in Fig. 1(b). Figure 1(c) shows a zoom-in image of the local structure of a superparamagnetic colloidal filament undergoes buckling instability in our experiment. Images of filament buckling are captured at a rate of 10 frames/sec using HCImage (Hamamatsu Corporation, Bridgewater, NJ). Contours of filaments are tracked using JFilament plugin [28,29] in Fiji, an open-source NIH software [30], which searches for the darkest ridges at the central line of each filament based on stretching and deforming open active contours.

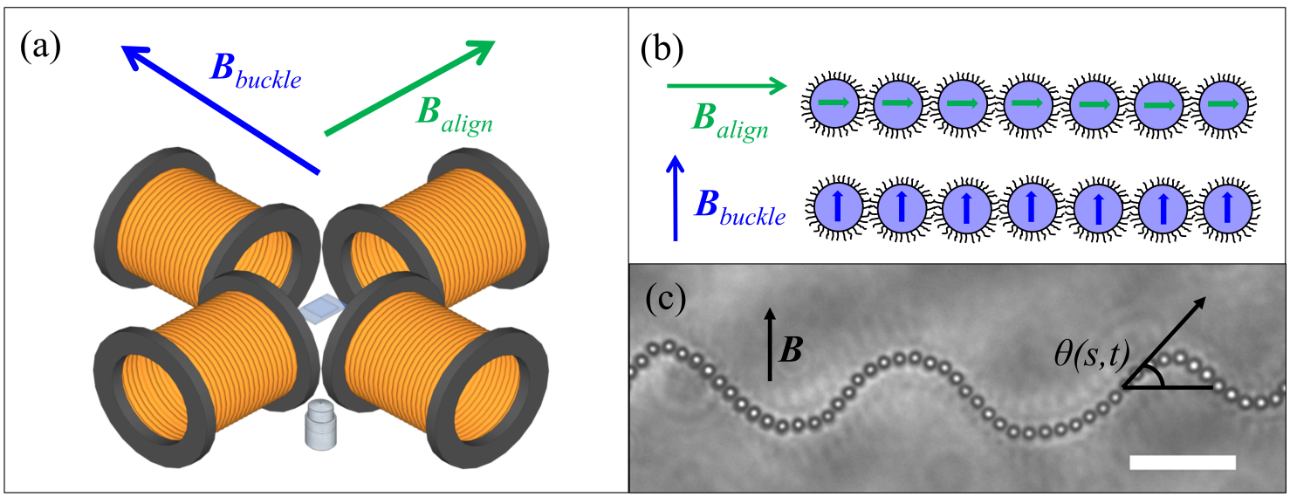

FIG. 1. (a) A schematic of the electromagnet microscopy setup used to image filament buckling. (b) The change of induced dipoles within the superparamagnetic filaments when the external field switched to perpendicular direction. (c) A zoom-in image of the local structure of a buckling superparamagnetic filament under orthogonal magnetic field. Scale bar, 10 μm.

III. THEORY

For an analytical description of the filament dynamics, we adopt the continuous worm-like chain model. Following the analysis of Roper *et al.*[19] and Cebers *et al.*[27], we consider an inextensible paramagnetic colloid-assembled filament of contour length L, diameter a, with $a/L << 1$. Its flexural rigidity is defined to be $\kappa = k_b T L_p$, where L_p is the filament persistence length and $k_B T$ is the thermal energy. The colloidal particles with magnetic susceptibility χ are of distance l away from their nearest neighbors. The deterministic energy functional *E(t)* for such a filament under a uniform field with a magnetic flux density $\boldsymbol{B}$ at certain time *t* is:

$$E(t) = \int_0^L \left[\boldsymbol{m}\cdot\boldsymbol{B}/2\mu_0 + \frac{\kappa}{2}\boldsymbol{r}_{,ss}{}^{\mathbf{2}} + \frac{1}{2}\Lambda(s,t)(\boldsymbol{r}_{,s}{}^{\mathbf{2}} - 1)\right] ds, \tag{1}$$

where $\boldsymbol{r}(s,t)$, parameterized by the arc length *s*, denotes the position vector of the filament. The first term of the integrand introduces the magnetic dipolar potential energy where μ_0 is the vacuum permeability. A simplified nearest neighbor mutual dipolar method [13,23] has been applied, and the magnetic moment per unit arc length $\boldsymbol{m} = \frac{\frac{4}{3}\pi a^3\chi/l}{1-\frac{4}{3}\left(\frac{a}{l}\right)^3\chi}B\boldsymbol{t} + \frac{\frac{4}{3}\pi a^3\chi/l}{1+\frac{2}{3}\left(\frac{a}{l}\right)^3\chi}B\boldsymbol{n}$, where $\boldsymbol{t}$ and $\boldsymbol{n}$ are the tangential and normal unit vectors in Frenet–Serret frame. The second term indicates the bending energy of an elastic beam, where $\boldsymbol{r}_{,ss}$ is the local curvature. Subscripts are used to denote partial derivatives. The last term has the Lagrange multiplier [32,33] $\Lambda(s,t)$ enforcing the constraint of local inextensibility $\boldsymbol{r}_{,s}{}^{\mathbf{2}} = 1$ and yielding the line tension.

Given that the motion of the colloidal filament operates in the low Reynolds number regime throughout the buckling process, inertia can be neglected so that the equation of motion for the filament is:

$$\zeta\frac{\partial\boldsymbol{r}}{\partial t} + \frac{\delta E}{\delta\mathbf{r}} = \boldsymbol{f}(s,t). \tag{2}$$

The contractile buckling dynamics is described by a balance of the dissipative hydrodynamic friction, where the friction coefficient is $\zeta = \zeta_{\parallel}\boldsymbol{tt} + \zeta_{\perp}\boldsymbol{nn}$, the conservative forces, as well as thermal fluctuations. For qualitative study, we make a Rouse dynamics simplification and assume local isotropic drag using slender-body theory [34] $\zeta_{\parallel} = \zeta_{\perp} = \zeta \sim 2\pi\eta/\log(2L/a) \sim \pi\eta$, and ignore long range hydrodynamic interactions. The fluid viscosity, measured to be η = 0.0022 *kg/m·s*, is used to account for the near wall effect [35]. To calculate the internal stresses $\boldsymbol{\sigma} = \frac{\delta E}{\delta\mathbf{r}}$ caused by the conservative forces, we utilize the principle of virtual work [36,37]. The detailed calculation can be found in the Appendix A. Combine Eq. (1) and Eq. (2), we have:

$$\zeta \boldsymbol{r}_{t,} + \frac{8\pi a^2\left(\frac{a}{l}\right)^4\chi^2 B^2}{3\mu_0\left(1-\frac{4}{3}\left(\frac{a}{l}\right)^3\chi\right)\left(1+\frac{2}{3}\left(\frac{a}{l}\right)^3\chi\right)} cos2\theta(s,t)\boldsymbol{r}_{,ss} + \kappa\boldsymbol{r}_{,ssss} + \left(\Lambda\boldsymbol{r}_{,s}\right)_{,s} = \xi, \tag{3}$$

where *θ(s,t)* is the tangent angle at arc length *s* and time *t*, as shown in Fig. 1(c). ξ denotes the thermal noise in the system. *cos θ* is a function of ***r*(*s,t*)**. We focus on the deterministic dynamics and the only randomness considered here is the initial stochastic transverse displacements along a straight contour. The tension *Λ* is determined from local inextensibility $\boldsymbol{r}_{ts} \cdot \boldsymbol{r}_s = 0$:

$$\Lambda = \left(\partial_{ss} - \left(\boldsymbol{r}_{,ss}\right)^2\right)^{-1}\left(\frac{8\pi a^2\left(\frac{a}{l}\right)^4\chi^2 B^2}{3\mu_0\left(1-\frac{4}{3}\left(\frac{a}{l}\right)^3\chi\right)\left(1+\frac{2}{3}\left(\frac{a}{l}\right)^3\chi\right)} cos2\theta(s,t)\left(\boldsymbol{r}_{,ss}\right)^2 + 4\kappa\boldsymbol{r}_{,ss}\boldsymbol{r}_{,ssss} + 3\kappa\left(\boldsymbol{r}_{,sss}\right)^2\right) \tag{4}$$

We can define dimensionless variables: $\tilde{s} = s/L, \tilde{t} = t/(\frac{\zeta L^4}{\kappa}), \tilde{\Lambda} = \Lambda/(\frac{1}{L^2\kappa})$ and the non-dimensionalized Eq. (3) becomes:

$$\boldsymbol{r}_{\tilde{t},} + Mncos2\theta(\tilde{s},\tilde{t})\boldsymbol{r}_{,\tilde{s}\tilde{s}} + \boldsymbol{r}_{,\tilde{s}\tilde{s}\tilde{s}\tilde{s}} + \left(\tilde{\Lambda}\boldsymbol{r}_{,\tilde{s}}\right)_{,\tilde{s}} = \boldsymbol{0}. \tag{5}$$

The equation of motion only depends on a single dimensionless number $Mn = \frac{8\pi a^2\left(\frac{a}{l}\right)^4\chi^2 B^2 L^2}{3\mu_0\kappa\left(1-\frac{4}{3}\left(\frac{a}{l}\right)^3\chi\right)\left(1+\frac{2}{3}\left(\frac{a}{l}\right)^3\chi\right)}$, which is the magnetoelastic number [23,31], representing the relative strength of magnetic to elastic forces.

IV. NUMERICAL METHODS

In order to quantitatively analyze the contractile buckling dynamics, a Brownian dynamics (BD) simulation [38] is performed. The colloidal filament is modeled as a bead-spring model, in which the colloidal particles are considered as the beads and the DNA linkers are modeled as Hookean springs. The contributing forces in this discretized system are magnetic dipolar interactions $\boldsymbol{F}^{mag}$, elastic bending forces $\boldsymbol{F}^{bend}$, hydrodynamic drag forces $\boldsymbol{F}^{hydro}$ and filament constraint forces $\boldsymbol{F}^{const}$. We also include thermal motion, which is denoted as a stochastic term Δx.

The deterministic governing equation for a buckling paramagnetic filament is:

$$\boldsymbol{F}_i^{\;mag} + \boldsymbol{F}_i^{\;bend} + \boldsymbol{F}_i^{\;hydro} + \boldsymbol{F}_i^{\;const} = m_i\frac{d^2\boldsymbol{r}_i}{dt^2} \cong \boldsymbol{0}, \tag{6}$$

where m_i and $\boldsymbol{r}_i$ are the mass and position of particle i, and N is the number of particles in the simulated filament. In Eq. (6), $\boldsymbol{F}_i{}^{mag}$ is calculated under mutual dipolar model [39]; $\boldsymbol{F}_i{}^{bend}$ is obtained using Euler beam theory; $\boldsymbol{F}_i{}^{const}$ are composed of stretching and repulsive terms, which obeys Hooks's law and the force-distance relation [40] of compressions between two polyelectrolyte coated particles, respectively. The detailed algorithm to calculate the values of $\boldsymbol{F}_i{}^{mag}$, $\boldsymbol{F}_i{}^{bend}$ and $\boldsymbol{F}_i{}^{const}$ can be found in Appendix B.

The hydrodynamic drag force on particle i is given by: $\boldsymbol{F}_i^{hydro} = -k_B T \boldsymbol{v}_i / \boldsymbol{D}_i$, where $\boldsymbol{v}_i$ is the relative velocity of the particle, and $\boldsymbol{D}_i$ is the diffusion constant, which is applied using a Rotne–Prager–Yamakawa tensor [41,42]. Utilizing the convention of Ermak and McCammon [43], the position vector $\boldsymbol{r}_i(t+\Delta t)$ of the bead i at time $t+\Delta t$ is related to the previous position vector $\boldsymbol{r}_i(t)$ as:

$$\boldsymbol{r}_i(t+\Delta t) = \boldsymbol{r}_i(t) - \left(\frac{\Delta t}{k_B T}\right) \sum_{j=1}^{N} \boldsymbol{D}_{ij} \cdot \boldsymbol{F}_j{}^{hydro} + \Delta x. \tag{7}$$

The stochastic term Δx is obtained utilizing a second-order Brownian dynamics algorithm [44], and the value can be calculated using Eq. (B7b).

Combining Eq. (6) and Eq. (7), the position of the particle i evolves as

$$\boldsymbol{r}_i(t+\Delta t) = \boldsymbol{r}_i(t) + \left(\frac{\Delta t}{k_B T}\right) \sum_{j=1}^{N} \boldsymbol{D}_{ij} \cdot \left(\boldsymbol{F}_j{}^{mag} + \boldsymbol{F}_j{}^{bend} + \boldsymbol{F}_j{}^{const}\right) + \Delta x_i, \tag{8}$$

The buckling motion of superparamagnetic filaments is simulated according to Eq. (8) with an optimized timestep of 5×10^{-6} sec.

V. RESULTS AND DISCUSSION

A. Comparing higher-order mode buckling dynamics with simpler buckling

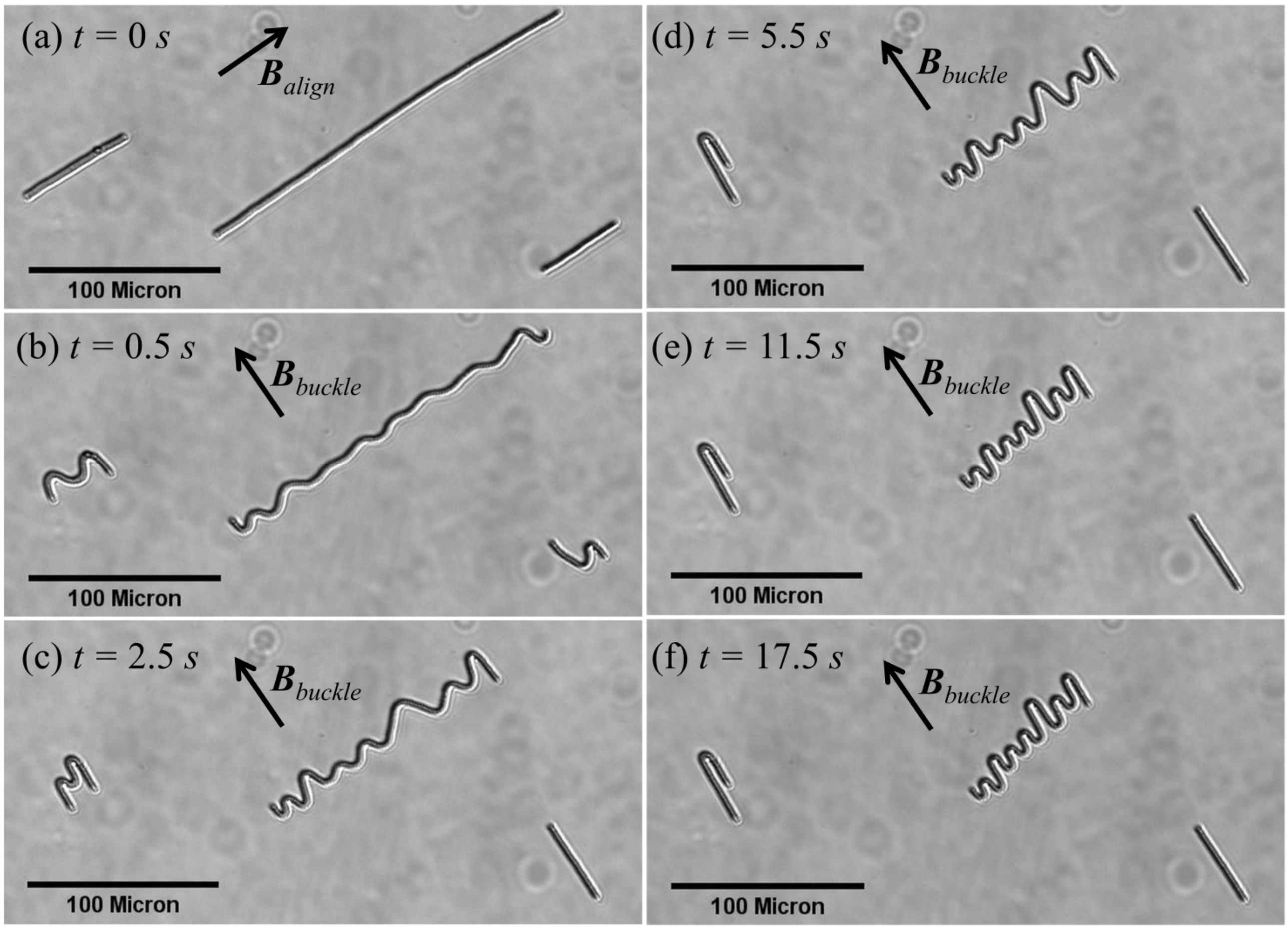

FIG. 2. A time series of snapshots of three superparamagnetic filaments buckles in experiment. The shortest filament realigns to the direction of the magnetic field 2.5 seconds after the buckling initiation (c); the filament with the medium length buckles into a quasi-stable hairpin shape 5.5 seconds from the direction switch of the external field (d); and it takes 11.5 seconds for the longest filament to fold into a 14-curve shapes (e). Persistence length of the filaments L_p = 1.20 mm. The buckling field strength B = 77 Gauss. Scale bar, 100 μm.

The dependence of filament length on buckling dynamics can be readily observed in Fig. 2. Short rigid filaments simply rotate to realign with the buckling magnetic field. With increasing filament length, the filament rotates to align with the buckling magnetic field direction but also exhibits a buckling mode, which is able to relax, as shown filament in the lower right corner of Fig. 2. For longer filaments, deformed configurations such as hairpin shapes are formed, with the two arms aligned with the new field direction. The filaments adopt a multi-mode buckled shape during the buckling process that rearrange into a single buckling mode. These hairpin shapes are quasi-stable over the timescale of the experiment. For much longer filaments, S-shapes or higher-order buckling mode shapes are observed. These structures take significantly longer to evolve and reach a quasi-stable configuration. The dynamics of these filaments is a result of the contractions along the original aligned direction rather than a rotational torque that acts to realign the filament with the orthogonal external field, resulting from the coupling of the transverse buckling and longitudinal displacement. These experimental results agree with Roper *et al*. [23] in that filaments with larger magnetoelastic numbers (*Mn*) tend to result in higher-order mode buckling shapes. It also provides a method to achieve complex folding of microfilaments. Notably, the buckling shapes in our experiments are saw-tooth rather than smooth curves, due to the large ratio of magnetic to elastic stresses in our experimental buckling conditions that provides large *Mn* for moderate filament length. We will focus on the long filaments below that are able to exhibit contractile buckling dynamics.

B. Three stages of contractile buckling dynamics

During contractile buckling, the magnetic potential energy is converted into elastic bending energy and dissipated through hydrodynamic friction. The repartitioning of magnetic and elastic energy, calculated using Eq. (1), continues throughout the entire process as the buckling modes developing and coarsening, as shown in Fig. 3(b). We identified three stages of contractile buckling behavior based on the energy evolution: initiation, development and decay.

During the pre-buckling stage (Fig. 3(b) section I), an alignment magnetic field is applied. The filament is extended in the direction of $\boldsymbol{B}_{align}$ due to the dipoles within the particles aligning with the external magnetic field. As a result, the elastic bending energy is small, and the magnetic potential energy is at its minimum. At $t=0$ in Fig. 3, when the field is switched to the perpendicular direction ($\boldsymbol{B}_{buckle}$) there is a rapid increase in the magnetic potential energy due to the instantaneous repulsive dipoles along the filament backbone. This marks the beginning of buckling instability and the starting point for the initiation stage.

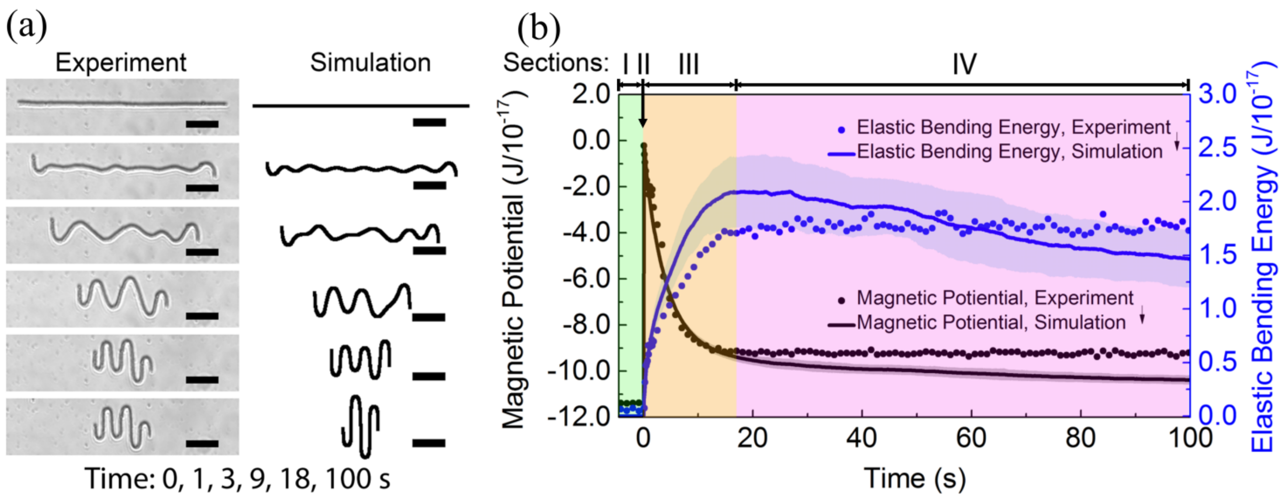

FIG. 3. Plot of (a) filament shape evolution captured in experiments (left) and numerical simulations (right) (b) magnetic potential and elastic bending energy evolution in a buckled filament when an orthogonal magnetic field is applied, based on both experiment and numerical simulation results. Persistence length of the filament $L_p = 1.33$ mm. The buckling field strength $B = 43$ Gauss. Scale bar, 24 µm. Filament length $L = 155$ µm. The numerical simulation result of energy evolution is calculated based on 100 runs. The shaded area indicates the error.

The straight configuration of the filament is unstable with respect to small transverse perturbation. Bulges start to develop on the filament contour. For short times, the transverse movement is achieved by taking advantage of the initial local thermal roughness without any longitudinal displacement. Buckling filaments in the initiation stage satisfy two criteria: nonlocal longitudinal movement is negligible comparing to transverse displacement and buckling curves have amplitude much smaller than wavelength.

Reflecting on the equation of motion, the line tension $\Lambda \sim 0$ and $\cos\theta \sim 1$. The dimensionless equation of motion Eq. (5) reduces to:

$$w_{\tilde{t},} + Mn w_{,\tilde{s}\tilde{s}} + w_{,\tilde{s}\tilde{s}\tilde{s}\tilde{s}} = 0. \tag{9}$$

where $w\,(\tilde{s}, \tilde{t})$ is the contour displacement, which has a direction perpendicular to the filament initial alignment. The initial instability is assessed using a linear stability analysis [20,23,45]. Proposing a small transverse deformation with normalized wavelength $\tilde{\lambda} = \lambda/L$ and a dimensionless growing rate $\tilde{\omega} = (\frac{\zeta L^4}{\kappa})\omega$: $w(\tilde{s}, \tilde{t}) \sim exp\,(\frac{2\pi i \tilde{s}}{\tilde{\lambda}} + \tilde{\omega}\tilde{t})$, and substituting it into the equation of motion Eq. (9), we arrive at a relation $\tilde{\omega}(\tilde{\lambda}) = \left(\frac{2\pi}{\tilde{\lambda}}\right)^2 Mn - \left(\frac{2\pi}{\tilde{\lambda}}\right)^4$. The fastest growing perturbation has the normalized growing rate $\tilde{\omega}_0 = Mn^2/4$ with a wavelength $\lambda_0 = \tilde{\lambda}_0 L = 2\sqrt{2}\pi L\sqrt{1/Mn}$, and the smallest existing wavelength $\lambda_c = \tilde{\lambda}_c L = 2\pi L\sqrt{1/Mn}$. Filaments with a length smaller than λ_c will rotate and realign to the orthogonal magnetic field without an initial buckling stage. It takes $\tau_0 = \frac{1}{\tilde{\omega}_0} \cdot (\frac{\zeta L^4}{\kappa}) < 0.1$ sec for the fastest growing deformation to be significant in this linearized dynamics, which can be served as the time span for initiation stage. As a result, the initial stage (Fig. 3(b) section II) is relatively short for buckling conditions studied in this paper and cannot be fully resolved with our experiments.

As the buckling modes continue to grow along the filament backbone, the buckling dynamics enter the development stage. The standard linear stability analysis no longer applies. Secondary and higher-order buckling bifurcations appear as the buckled curves coarsen, resulting in an increase in their wavelength and amplitude, as shown in Fig. 3(a). The elastic energy gradually increases as new curves develop and rearrange along the filament backbone, while the magnetic potential decreases due to the realignment of the dipoles (Fig. 3(b) section III). The decrease in the magnetic potential energy is much larger than the gain in elastic bending energy, which is needed to satisfy the experimental requirement of large *Mn* and moderate filament length. The majority of the magnetic potential energy is dissipated through hydrodynamic friction. With increasing time, the variance in elastic bending energy increases, which is an effect of stochasticity in the rearrangements among the buckling modes that occur in this system. The experimental data and simulation agree well in the energy plot with the exception that the bending energy calculated from experiments is typically smaller than that observed from simulations. This is likely due to small heterogeneities in the experimental filaments that encourage early coarsening of curves. Detailed discussion of the dynamics in the development stage will be given in the next section.

The buckling process enters decay stage when the curves on the filament contour reach a balance between the magnetic and elastic forces. The relaxation time of the buckling mode exceeds its formation time, resulting in a quasi-stable configuration. Comparing the experiment and simulation data in Fig. 3 (a), the buckled filament appears to have a stable shape after reaching the decay stage in experiment, while in simulation, the buckled filament continues to relax. A similar phenomenon is observed in the energy evolution in Fig. 3 (b) section IV, whereby energy curves from experimental data reach a plateau while in simulations, the magnetic potential energy continues to decrease, and the elastic bending energy also decreases after reaching its maximum value. The anomalous stability of the experimental shapes indicates a deviation of experimental filament condition at quasi-stable stage from the assumption of ideal paramagnetic colloidal filaments with uniform elastic modulus. The magnetic heterogeneity within the paramagnetic colloidal particles and the possible nonlinear elastic deformation [23] may be responsible for this deviation.

C. Analysis of nonlinear dynamics of contractile buckling

In the development stage, the paramagnetic colloidal filaments exhibit inhomogeneous contractile buckling dynamics. Due to the inextensibility of the filament, a buckling mode on the filament backbone must decrease the filament length along the primary alignment axis to grow and evolve. The transverse movement is coupled with the longitudinal one. The buckling modes in the middle section of the filament are typically confined so the free tail ends of the filament must pull towards the center. Hydrodynamic friction limits the development of buckling modes in the center section of the filament. Similar to the inhomogeneous recoil dynamics of a suddenly released prestretched polymer [37,46,47], the non-uniform friction leads to an inhomogeneous dynamics in our studied system. As shown in Fig. 4(a), the amplitudes of buckling curves increase slower with time when approaching the center of the filament.

There are two regimes along the contour of a buckling filament in early development stage, which can be observed in Fig. 4(a). More obviously, when the tangent angle is used to describe the evolving shape in Fig. 4(b), the region with similar tangent angle fluctuations is separated by the white dash line from the region where the tangent angle fluctuation is greatly amplified. Located at the center of the filament, the bulk regime is defined as the segment of filament that does not exhibit significant longitudinal movement at any given time. On the other hand, the end regime is defined as the tail sections of a filament that exhibit significant longitudinal displacement. Figure 4(c) shows there is a relatively clear front that separates the bulk from the end regime, especially at smaller timescales, and from this graph, we can track a decay length at which the longitudinal speed drops to half of its maximum value. We find that at moderate *Mn*, the length of the propagation layer, corresponding to the white dashed line in Fig. 4(b), is approximately double the decay length mentioned above. With increasing time, the propagation front of the buckling modes moves from the filament ends to the center. After the end regime propagates to the center of the filament, the contraction of different segments along the filament starts to become more uniform and the inhomogeneity of the contractile movement gradually reduces.

To investigate the wavelength evolution of the contractile buckling dynamics, a standard Fourier analysis is applied onto the series of buckling shapes. The Fourier mode amplitude of the buckling filament, normalized by the maxium mode amplitude, is plotted out as a function of the normalized wave number $\tilde{k} = 2L/\lambda$ and time t in Fig. 4(d). The dominant $\tilde{k}$ has a normalized Fourier mode amplitude of 1. The initiation stages can be observed in this plot. At small timescales $t < \tau_0$, the dominant $\tilde{k}$ remains constant $2L/\lambda_0 = \sqrt{Mn}/\sqrt{2}\pi$. Exiting the initiation stage, the dominant $\tilde{k}$ evolution demonstrates an asymptotic power law of -4. This power law is well followed until $t \sim 2$ sec, which is approximately the time when the end regime covers half of the contour length. In the later development stage, the dominant $\tilde{k}$ deviates from the power law of -4 and the decreasing of $\tilde{k}$ gradually slows.

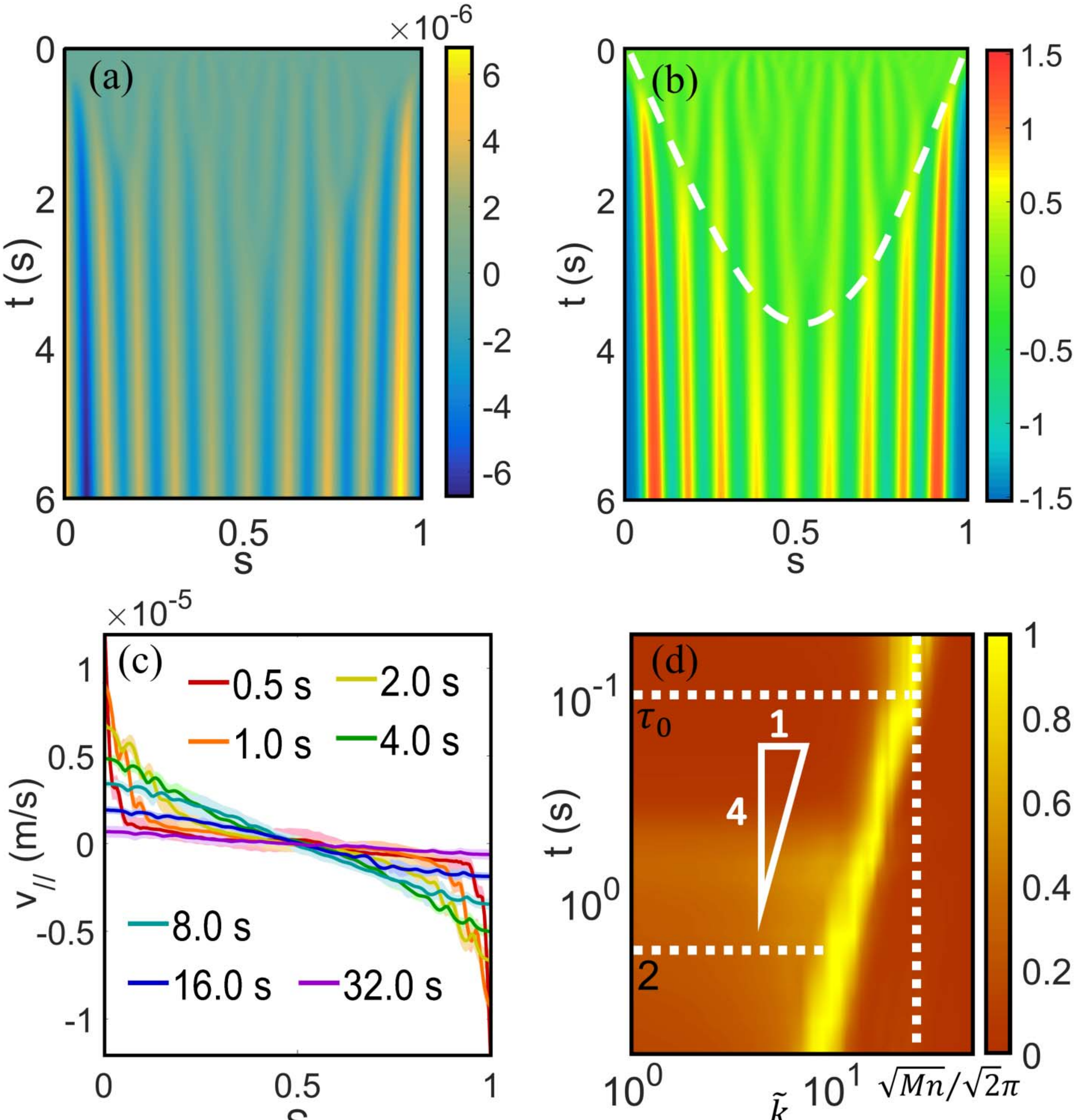

FIG. 4. The development stage of simulated contractile buckling dynamics of a paramagnetic colloidal filament with filament length L = 246 μm, persistence length L_p = 1.33 mm. The buckling field strength is

43 Gauss. (a,b) Colormaps showing the relationship between (a) transverse displacement from the initial aligned configuration and (b) tangent angle, respectively, along the filament and normalized contour length *s* (by filament contour length) as well as time *t*. (c) Contraction speed $v_{\parallel}(s,t)$ in the longitudinal direction along the filament backbone at different times. Results based on 100 runs. The shaded area indicates the error. (d) log-log colormap of normalized fourier modes amplitude of the filament shape (by the maxium mode amplitude) with the normalized wave number $\tilde{k}$ and time *t*.

The transverse buckling dominated bulk regime is responsible for the asymptotic power law of -4 of the wave number in Fig. 4(d). Here we show that the wavelength evolution obeys $\lambda \sim \lambda_0 (t/\tau_0)^{1/4}$ when the buckling dynamics of paramagnetic filament exhibits negligible longitudinal motion. The time and wavelength of the filament, τ_0 and λ_0, respectively, denote when the buckling dynamics exit the initiation stage and enter the development stage. Analytically, these two parameters obey $\lambda_0 \sim 2\sqrt{2}\pi L\sqrt{1/Mn}$ and $\tau_0 \sim \frac{4\zeta L^4}{\kappa M n^2}$, which are obtained from the linear stability analysis. Their exact values are affected by the initial thermal fluctuation conditions.

To prove the statement above, a numerical method is applied. We designed a simplified buckling system with no global longitudinal movement, by virtually connecting the two ends of the filament to eliminate the significant end deformation that leads to contraction. The length of the simulated chain is set to be long enough so that the coupled ends do not significantly influence the transverse buckling dynamics. The initial filament shape is set to have small random undulations with a hidden contour of $\epsilon =$ 2.8% to enable buckling. Figure 5(a) shows the evolution of the filament conformation during the buckling process without contraction. Following Ref. [45], wavelength λ of the filament is calculated using slope-slope correlation method and root mean square amplitude *w* is measured to quantify the transverse displacement. The slope-slope correlation function of distance *n* along the contour and time *t* is defined as:

$$K_{tt}(n,t) = < \boldsymbol{t}(s = s_0 + n, t) \cdot \boldsymbol{t}(s = s_0, t) >, \tag{10}$$

where the symbol <…> denotes the ensemble spatial average over the contour length of the filament, $\boldsymbol{t}(s,t)$ is the tangent unit vector at the arc length s and the time $\boldsymbol{t}$**.** The wavelength λ is four times the value of the first zero $n_1(t)$ of $K_{tt}(n,t)$. The wavelength and amplitude are normalized by λ_0 and w_0, respectively, which are the values of λ and w at the end of the initiation stage. In experiment and numerical simulation, w_0 and λ_0 are determined as the value at the time when wavelength starts to increase significantly. Figure 5(c) and (d) show the simulated wavelength and amplitude evolution of the simplified undulance dominated system, and a power law of 1/4 is obtained for both. The rescaled slope-slope correlation function at different time collapses into a single curve, as shown in Fig. 5(b), which indicates the time developing buckling conformation of paramagnetic filament exhibits self-similarity. This in return supports that there is a dynamic scaling for the buckling shape evolution. In comparison to the buckling dynamics without contraction, data from an experiment with similar conditions ($Mn = 1.47 \times 10^5$) but allowing free-end contraction is plotted out in Fig. 5(c) and (d). Both the amplitude and wavelength evolution curves from experimental data deviate from the power law of ¼, due to the coupling of contraction dynamics and transverse buckling relaxation in the end regime. Notably, we applied different methods to analyze the wavelength evolution in Fig. 4(d) and Fig. 5(d). In Fig. 4(d), the normalized Fourier modes amplitude with the mode number and time are plotted out. When the bulk regime is dominant, the dominant amplitude mode (which corresponds to the mode of the bulk regime), results in a 1/4 scaling at early buckling times. For Fig. 5(d), the slope-slope correlation method is applied to calculate the characteristic wavelength, which is affected by both the bulk and the end regime, so the scaling deviates from 1/4, even at initial buckling timescales. The overall trend of the wavelength evolution in early development stage is the same in both figures, where the contraction dynamics slows down the transverse relaxation.

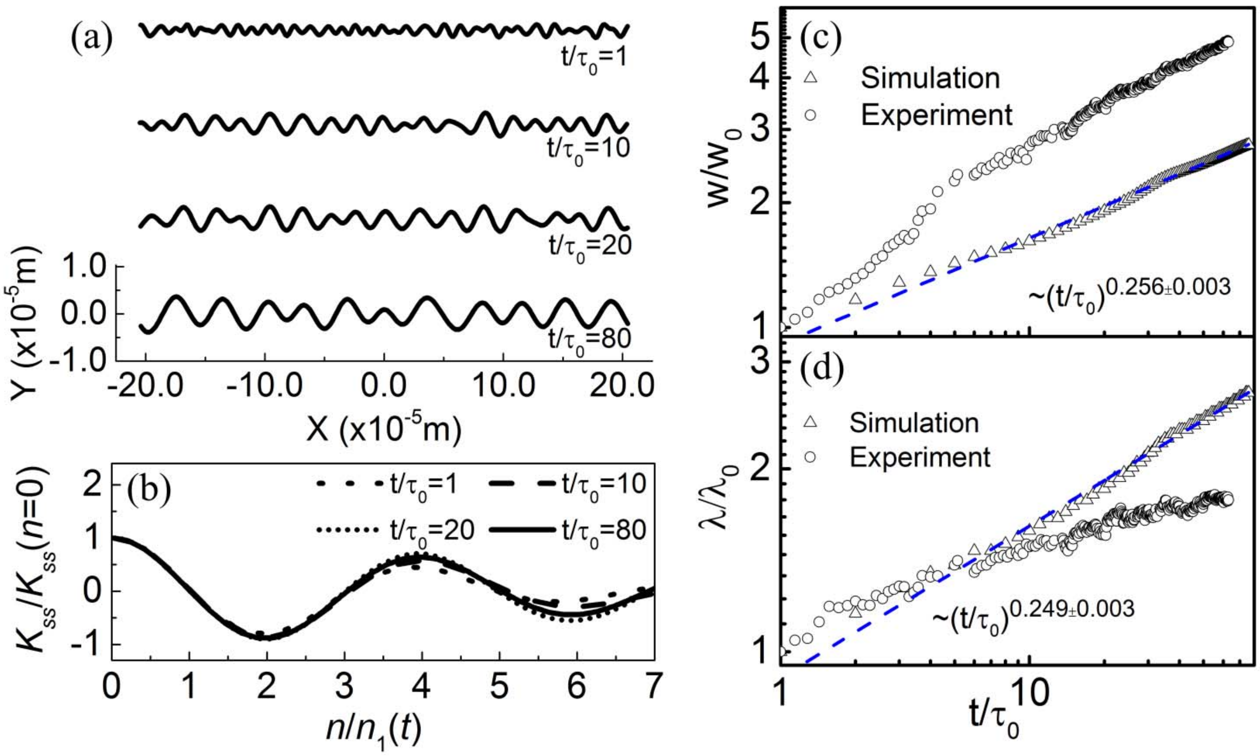

FIG.5. (a) Snapshots of the simulated filament conformation during the orthogonal magnetic field induced buckling process without contraction. The buckling process has $Mn = 1.47 \times 10^5$, the persistence length of the filament L_p = 1.33 mm, and the buckling field strength B = 77 Gauss. (b) The rescaled slope-slope correlation function of buckling shapes in (a) collapse onto a single curve. (c,d) The temporal evolution of (c) normalized amplitude w/w_0 and (d) normalized wavelength λ/λ_0 of the buckling filament. Simulation system is restricted to only transverse displacement by coupling the dynamics of the free ends together. Experimental results from system of the same buckling condition with same *Mn* but the ends of the filament remain free.

To understand this nontrivial scaling relation within the bulk regime, we present a scaling analysis. Although contractile buckling of paramagnetic filaments is intrinsically nonlinear, the dynamics within the bulk regime can be predicted analytically using a linear calculation within the weakly bending limit. Neglecting the axial movement, the dimensionless equation of motion Eq. (5) in the transverse direction becomes,

$$w_{\tilde{t},} + Mncos2\theta(\tilde{s},\tilde{t})w_{,\tilde{s}\tilde{s}} + w_{,\tilde{s}\tilde{s}\tilde{s}\tilde{s}} + \left(\tilde{\Lambda} w_{,\tilde{s}}\right)_{,\tilde{s}} = 0, \tag{11}$$

where $w\ (\tilde{s},\tilde{t})$ is the normal displacement. In the weak bending limit, $\epsilon = 1 - (r_{\parallel}(\tilde{s} = 1, \tilde{t} = 0) - r_{\parallel}(\tilde{s} = 0, \tilde{t} = 0))/\boldsymbol{L} \ll 1$, where $r_{\parallel}\ (\tilde{s},\tilde{t})$ is the position on the axial direction, ϵ is the normalized contour length stored in the lateral undulations. Since $w_{,\tilde{s}}$ is of order $O(\epsilon^{1/2})$ and $\tilde{\Lambda}_{,\tilde{s}}$ is of order $O(\epsilon)$, Eq. (11) is to the leading order $O(\epsilon^{1/2})$ given by a balance of hydrodynamic drag force, effective line tension, and bending force:

$$w_{\tilde{t},} + f(\tilde{t})\, w_{,\tilde{s}\tilde{s}} + w_{,\tilde{s}\tilde{s}\tilde{s}\tilde{s}} = 0, \tag{12}$$

where the spatial average $f(\tilde{t}) = \int_0^1 d\tilde{s}(Mncos2\theta(\tilde{s},\tilde{t}) + \tilde{\Lambda})$. Consider a transverse buckling dominated filament governed by the balance of the drag force with bending force and tension (or elastic stretching force for extensible filaments). Evidence from previous studies [48–50] shows that the bending term and tension term are of the same order, as long as there is no significant longitudinal movement in the buckling dynamics. Note that when the magnetic field induces buckling within the bulk regime, the contribution of magnetic interactions is absorbed into the line tension term in the governing equation described by Eq. (12). The bending force and effective line tension are of the same order of magnitude, analogous to previously published research results mentioned above. The scaling analysis of Eq. (12) has the form:

$$\frac{\bar{w}}{\tilde{t}} \sim \frac{\bar{w}}{\tilde{\lambda}^4} + \frac{\bar{w}}{\tilde{\lambda}^2} f(\tilde{t}), \tag{13}$$

where $\bar{w}$ and $\tilde{\lambda}$ are the characteristic curve amplitude and normalized wavelength, respectively. The bending force ($\propto \frac{\bar{w}}{\tilde{\lambda}^4}$) is comparable to the induced tension in the filament ($\propto \frac{\bar{w}}{\tilde{\lambda}^2} f(\tilde{t})$) resulting from the magnetic dipolar interactions and the inextensibility of the backbone, as long as the longitudinal motion is negligible comparing to the transverse motion. Therefore, $f(\tilde{t}) \sim \tilde{\lambda}^{-2}$ is achieved and $\tilde{\lambda} \propto t^{1/4}$. For a more comprehensive understanding, Hallatschek's theoretical analysis [51] for the initially buckled incompressible rod in the uniformly buckled bulk regime in viscous media can be extended to our system: the ubiquitous -1/2 power-law temporal decay of the tension and the 1/4 power law of wavelength evolution are quantitatively derived. Briefly, Eq. (12) has a group of solutions with separated variables of wave and temporal evolving mode amplitudes. Mode amplitudes are related to the line tension force history, . The stored contour length can be separated into different buckling modes whose value can also be expressed in mode amplitudes. Therefore, the mode amplitudes relate the conservation of stored contour length and the time integral of line tension together, which results in a -1/2 power-law temporal decay of the tension and therefore a 1/4 power law of wavelength evolution. The amplitude evolution in the bulk regime of the magnetic field induced buckling system follows the same power law of 1/4 due to its coupling with wavelength to maintain a constant .

For the transverse dynamics dominated bulk regime in the early development state, the far-field hydrodynamic interactions do not significantly affect the dynamics. Reflecting on the simulation result of the filament buckling without contraction, it follows the 1/4 scaling law concluded from analytical theory. For late development state, however, far-field hydrodynamic interactions cannot be neglected. The analytical method without long range hydrodynamic interactions only gives a qualitative description of the dynamics.

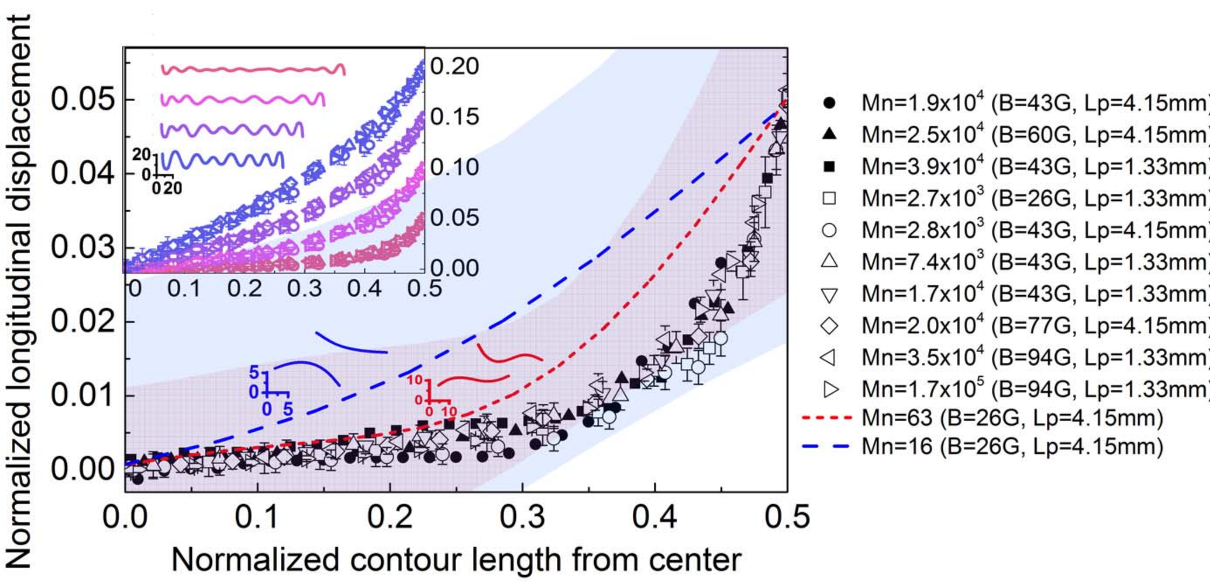

FIG.6. Normalized longitudinal displacement along the filament backbone at (main plot) 10% end-to-end contraction ratio and (inset) four different end-to-end contraction ratios of 10%, 20%, 30% and 40%, with system of different *Mn*. The normalized longitudinal displacement is defined as the displacement of a small segment on the filament at a particular time from the initial straight configuration normalized by the length of the filament, and the normalized contour length from center is defined as the distance between the segment and the center of the filament normalized by the length of the filament. Both experiment (solid points) and numerical simulation (hollow points) results of higher-order buckling (*Mn*: 2.7×10^3 - 1.7×10^5, or approximately 8 - 45 buckling modes) are plotted out. The numerical simulation result is an average of 100 runs with the error bars indicating the variance. The first (*Mn* = 16) and second (*Mn* = 63) mode buckling results are also included in the main plot with two example buckling shapes for each case next to the result curves and the shaded area (light blue for *Mn* = 16 and light pink for *Mn* = 63) indicating the error. Example buckling conformations of 10%, 20%, 30% and 40% end-to-end contraction ratios of a *Mn* = 1.7×10^4 system is shown at the top left corner of the inset.

The nonlinear longitudinal movement is the key to the inhomogeneity of the development stage contractile buckling dynamics. In the early development stage where the end and bulk regimes coexist, significant inhomogeneous contraction within the propagation layer leads to a non-uniform buckling conformation. In the late development stage, where the bulk regime vanishes, the nonlinear longitudinal movement along the filament contour remains and continue to contribute to the non-uniform dynamics. Here the longitudinal displacement of the filament can be used as an indicator for inhomogeneous dynamics. The full nonlinear equation of motion Eq. (3) needs to be considered. Figure 6 plots out the normalized longitudinal displacement along the filament contour for different contractile buckling experiments. The nonlinearity of the dynamics increases as the longitudinal displacement curve deviates from the straight line.

In early development stage, higher-order buckling dynamics tend to have similar inhomogeneous contractions; while for smaller mode number buckling systems, the contraction dynamics become more linear as the buckling mode number decreases. As shown in Fig. 6, at moderate *Mn* (2.7×10^3 - 1.7×10^5) that covers most of higher-order mode contractile buckling experiments considered in this paper, the longitudinal displacement curves with respect to filament contour under different experimental conditions collapse onto a single curve, given by the same 10% end-to-end contraction ratio. However, for smaller *Mn* (*Mn* = 16, 63), which is characteristic of the smaller buckling modes, the curve tends to approach a straight line connecting the center zero displacement with the largest displacement at the end, which is indicative of pure rotation at conditions with *Mn* close to zero. The first mode buckling has an almost linear longitudinal displacement (blue dashed line in Fig. 6) and the second mode buckling (red short dashed line in Fig. 6) shows increase longitudinal nonlinearity. With increasing *Mn*, the change in contraction linearity becomes less sensitive to the increase in the mode number and the longitudinal dynamics along the filament backbone are similar for higher-order mode buckling.

Thermal fluctuations have a significant impact on the longitudinal dynamics of the contractile buckling system with small buckling modes. Fig. 6 shows that at small *Mn*, there is a large variance in the longitudinal displacement. With increasing *Mn*, this variance decreases and from our numerical simulation results, the variance becomes negligible when the buckling mode number is greater than 8 (*Mn* $< 2.7\times10^4$). The variance reveals the influence of thermal fluctuations on the filament buckling dynamics. For the first and second mode buckling dynamics, thermal fluctuations have a considerable impact on the longitudinal movement. For buckling dynamics with higher modes, the effect of stochasticity averages out among all the buckling modes and the collective result of longitudinal movement is not significantly affected.

The nonlinearity of higher-order mode contractile buckling initially increases and then decreases throughout the development stage. For a small contraction ratio such as 10%, as shown by the black data points in Fig. 6, the longitudinal displacement curve with small values (0-0.3) of the contour length from center is approximately zero. When the end-to-end contraction ratio increases, the value of the previously zero longitudinal displacement increases until the entire longitudinal displacement curve becomes positive except at the center point, which marks the end of the early development stage (around 20% end-to-end contraction). The nonlinearity of buckling shapes increases monotonically in the early development stage as the longitudinal displacement curves continues to deviate from the straight line. After that, the buckling dynamics enter the late development stage where the longitudinal movement starts to slow down near the end region. The nonlinearity decreases as the contraction ratio increases and becomes more linear, as shown by the 30% and 40% end-to-end contraction data given by the purple and blue data points in the inset of Fig. 6, respectively. The buckling shapes will continue to become more uniform until reaching the decay stage, which is the end of the continuous longitudinal movement.

VI. CONCLUSION

In this paper we have described the contractile buckling dynamics of superparamagnetic filament using an orthogonal magnetic field in aqueous media. As a result of the competition between magnetic interactions, elastic bending forces and hydrodynamic friction, the paramagnetic filament undergoes an intrinsically nonlinear relaxation process. Flexible magnetic filaments under a strong external field (large *Mn*) tend to have higher-order buckling with contractions along the original aligned direction in the early stage, rather than rotations to realign with orthogonal external field. For these higher-order buckling dynamics, we identified three stages: initiation, development and decay. The initiation stage represents the onset of magnetoelastic buckling instability. Transverse dynamics is dominant in initiation stage and periodic higher-order mode buckling curves are formed. Following bucking initiation, the development stage is a transient state due to the competition between magnetic, elastic, and hydrodynamic forces. Here, small buckling curves coarsen into larger folds and the transverse displacement increases, while the filament experiences rapid contraction in longitudinal direction. In the final decay stage, the filament reaches a balance between the magnetic and elastic forces. The relaxation time of a buckling mode exceeds its formation time, resulting in the filament obtaining a quasi-stable buckling shape. Brownian dynamic simulations prove to be useful to studying the contractile buckling dynamics, and match well with experimental results. Comparing to the wrinkling of vesicles in elongation flow [52,53] which also demonstrates the three dynamical stages, the system studied in this paper exhibits nonlinear contractile buckling. With experimental, theoretical as well as numerical approaches, we analyze the inhomogeneous coarsening of the buckling curves. Two regimes in the early development stage are identified: a bulk regime in the center of the filament where longitudinal movement is negligible and an end regime where contraction movement is significant. We demonstrated the asymptotic power law of 1/4 for buckling wavelength coarsening in the early development stage is due to the transverse buckling dominated bulk regime. We also observed for moderate *Mn*, the inhomogeneity of higher-order mode contractile buckling for different conditions are similar and following a first increase and then decrease trend until approaching the decay stage.

ACKNOWLEDGMENT

We thank Dr. Julie Byrom for her assistance in filament preparation experiments and valuable discussions, and Ziyi Zhu for his insights and bringing the modified thermal fluctuations calculation in Ref. 44 to the simulation algorithm. The simulations are supported by NIH award NCRR S10RR02950, an IBM Shared University Research (SUR) Award in partnership with CISCO, Qlogic and Adaptive Computing, and Rice University.

APPENDIX A: INTERNAL STRESSES CALCULATION [37]

Internal stress σ and the deterministic functional of the filament *E* are related by

$$E = \int_0^L ds\boldsymbol{\sigma}(s)\boldsymbol{r}(s), \tag{A1}$$

at a particular time *t*. Introducing a virtual displacement $\delta\mathbf{r}$ which is an assumed infinitesimal change of the filament position rector, the new filament position vector becomes $\hat{\boldsymbol{r}}(s) = \boldsymbol{r}(s) + \delta\boldsymbol{r}(s)$. Substituting $\boldsymbol{r}(s)$ with $\hat{\boldsymbol{r}}(s)$ in Eq. (A1) and the change in energy functional reads $\delta E = \int_0^L ds\boldsymbol{\sigma}(s)\delta\boldsymbol{r}(s)$. From Eq. (1), $\delta E = \int_0^L ds(C_1 + C_2((\boldsymbol{r}_{,s} + \delta\boldsymbol{r}_{,s})\boldsymbol{e})^2 + \frac{\kappa}{2}(\boldsymbol{r}_{,ss} + \delta\boldsymbol{r}_{,ss})^2) - \int_0^L ds(C_1 + C_2(\boldsymbol{r}_{,s} \cdot \boldsymbol{e})^2 + \frac{\kappa}{2}\boldsymbol{r}_{,ss}{}^2)$ $= \int_0^L ds(2C_2(\boldsymbol{r}_{,s}\boldsymbol{e})(\delta\boldsymbol{r}_{,s}\boldsymbol{e}) + \kappa\boldsymbol{r}_{,ss}\delta\boldsymbol{r}_{,ss})$, where $\boldsymbol{e}$ is the unit vector in the same direction as the external magnetic field, constants $C_1 = \frac{2\pi a^3 \chi B^2 (\frac{4}{3}(\frac{a}{l})^3 \chi - 1)}{3\mu_0 l \left(1-\frac{4}{3}(\frac{a}{l})^3 \chi\right)\left(1+\frac{2}{3}(\frac{a}{l})^3 \chi\right)}$ and $C_2 = -\frac{4\pi a^2 (\frac{a}{l})^4 \chi^2 B^2}{3\mu_0 \left(1-\frac{4}{3}(\frac{a}{l})^3 \chi\right)\left(1+\frac{2}{3}(\frac{a}{l})^3 \chi\right)}$. The implicitly expressed line tension Λ is not included here and will appear later in this calculation. Given the inextensibility of the filament backbone, we have $\boldsymbol{r}_{,s} = \boldsymbol{t}$ and $\delta \boldsymbol{r}_{,s} = C(s)\boldsymbol{n}$. As a result,

$$\delta E = \int_0^L ds(C_2 sin2\theta \delta \boldsymbol{r}_{,s} + \kappa \boldsymbol{r}_{,ss} \delta \boldsymbol{r}_{,ss}) = \int_0^L ds \boldsymbol{\sigma} \delta \boldsymbol{r}, \tag{A2}$$

which can be rearranged to be:

$$\int_0^L ds[C(s)(-C_2 sin2\theta + \kappa \boldsymbol{r}_{,sss} + \int_0^s d\bar{s}\boldsymbol{\sigma}) \cdot \boldsymbol{n}] + const. = 0, \tag{A3}$$

in which const. is only related to boundary conditions. To satisfy Eq. (A3) under different virtual displacement, that is, different function *C(s)*, $(-C_2 sin2\theta + \kappa \boldsymbol{r}_{,sss} + \int_0^s d\bar{s}\boldsymbol{\sigma}) \cdot \boldsymbol{n}$ has to vanish. As a result,

$$-C_2 sin2\theta + \kappa \boldsymbol{r}_{,sss} + \int_0^s d\bar{s}\boldsymbol{\sigma} = g(s)\boldsymbol{r}_{,s} \tag{A4}$$

where $g(s) = -\Lambda(s)$, and $\Lambda(s)$ has the physical meaning of the line tension and enforcing the constraint of local inextensibility. The internal stress can be written as:

$$\boldsymbol{\sigma} = -2C_2 cos2\theta \boldsymbol{r}_{,ss} + \kappa \boldsymbol{r}_{,ssss} + \left(\Lambda \boldsymbol{r}_{,s}\right)_{,s}. \tag{A5}$$

APPENDIX B: BROWNIAN DYNAMIC SIMULATION ALGORITHM

The discretized version of magnetic force [54] on particle *i* can be approximated as:

$$\boldsymbol{F}_i^{mag} = \sum_{j=1, j\neq i}^{N} \frac{3\mu_0}{4\pi r^5}\left[(\boldsymbol{m}_i \cdot \boldsymbol{r}_{ij})\boldsymbol{m}_j + (\boldsymbol{m}_j \cdot \boldsymbol{r}_{ij})\boldsymbol{m}_i + (\boldsymbol{m}_i \cdot \boldsymbol{m}_j)\boldsymbol{r}_{ij} - \frac{5(\boldsymbol{m}_i \cdot \boldsymbol{r}_{ij})(\boldsymbol{m}_j \cdot \boldsymbol{r}_{ij})}{\boldsymbol{r}_{ij}^2}\boldsymbol{r}_{ij}\right], \tag{B1}$$

where $\boldsymbol{r}_{ij}=\boldsymbol{r}_j-\boldsymbol{r}_i$ is the center to center vector of the two particles. Applying mutual dipolar model [39], the magnetic dipole moment for particle *i* has an expression of $\mathbf{m}_i = \frac{4}{3}\pi a^3 \chi_{eff}\left(\mathbf{B}/\mu_0 + \sum_{j=1, j\neq i}^{N} \mathbf{H}_{dip}\right)$, where $\boldsymbol{H}_{dip} = \frac{1}{4\pi}\left(\frac{3\boldsymbol{r}_{ji}(\boldsymbol{m}_j \cdot \boldsymbol{r}_{ji})}{|\boldsymbol{r}_{ji}|^5} - \frac{\boldsymbol{m}_j}{|\boldsymbol{r}_{ji}|^3}\right)$ is the induced magnetic field by the other dipole *j*.

Considering the elastic bending forces, the colloidal filament is simplified to an Euler beam. The discretized elastic bending energy U^{bend} of the DNA linkers between neighboring particles can be expressed using beam theory:

$$U^{bend} = \frac{L_p k_B T}{l} \sum_{i=1}^{N} p_i (1 - \boldsymbol{t}_{i,i+1} \cdot \boldsymbol{t}_{i-1,i}),$$

$$p_i = \begin{cases} 1; i = 2,3, \dots N-1 \\ 0; i = 1, N \end{cases}, \tag{B2}$$

where $\boldsymbol{t}_{ii}$ is the unit vector of $\boldsymbol{r}_{ij}$. Therefore, the bending force between particle i and its adjoining particle j $\boldsymbol{F}_{ij}{}^{bend}$ is given by [38]:

$$\boldsymbol{F}_i{}^{bend} = \frac{L_p k_B T}{l^2} (p_{i-1}\boldsymbol{t}_{i-2,i-1} - \left(p_{i-1}\boldsymbol{t}_{i-2,i-1} \cdot \boldsymbol{t}_{i-1,i} + p_i + p_i \boldsymbol{t}_{i-1,i} \cdot \boldsymbol{t}_{i,i+1}\right)\boldsymbol{t}_{i-1,i}$$

$$+\left(p_i \boldsymbol{t}_{i-1,i} \cdot \boldsymbol{t}_{i,i+1} + p_i + p_{i+1}\boldsymbol{t}_{i,i+1} \cdot \boldsymbol{t}_{i+1,i+2}\right)\boldsymbol{t}_{i,i+1} - p_{i+1}\boldsymbol{t}_{i+1,i+2}),$$

$$p_i = \begin{cases} 1; i = 2,3, \dots N-1 \\ 0; i = 1, N \end{cases}. \tag{B3}$$

Filament constraint forces contain repulsive and stretching forces:

$$\boldsymbol{F}_i^{const} = \boldsymbol{F}_i^{rep} + \boldsymbol{F}_i^{strech}, \tag{B4}$$

The charge and steric repulsive force $\boldsymbol{F}^{rep}$ of the neighboring particle i and j are caused by the DNA-grafted surfaces, and can be written in terms of the surface-to-surface distance D^s_{ij} of the colloidal particles i and j as follows [40],

$$\boldsymbol{F}_i^{rep} = \Sigma_j \left(C_1(1+\ln(18\ \text{Å})-\ln(D^s_{ij}))/ {D^s_{ij}}^2 + 2C_2 D^s_{ij}\right),$$

$$i = \begin{cases} 1; j = 2 \\ 2,3, \dots N-1; j = i \pm 1. \\ N; j = N-1 \end{cases} \tag{B5}$$

where the constants C_1 and C_2 are influenced by the molecular weight of the DNA linkers, and the concentration and valence of the surrounding ionic medium. In this study, the constants are treated as fit parameters to the experimental data obtained using the method described by Li *et al*. [55].

The stretching force $\boldsymbol{F}_i^{stretch}$ between neighboring particle i and j obeys Hooks's law,

$$F_i^{stretch} = -k \sum_j (l_{ij} - l)^2,$$

$$i = \begin{cases} 1; j = 2 \\ 2,3, \dots N-1; j = i \pm 1. \\ N; j = N-1 \end{cases} \tag{B6}$$

where $(l_{ij}$-$l)$ is the deviation of the distance from the equilibrium distance and the constant k is set to 5.0×10^{-3} N/m which is large enough to approximate an inextensible filament.

For the stochastic term corresponding to Brownian motion, different approaches [44,56,57] have been reported to represent thermal fluctuations both qualitatively and quantitatively. Here we utilize a second-order Brownian dynamics algorithm [44] to compute the stochastic displacement, Δx_i, of the colloidal particles that qualitatively represents the thermal motion:

$$\boldsymbol{r'}_{\boldsymbol{i}}(t+\Delta t) = \boldsymbol{r}_{\boldsymbol{i}}(t) + \left(\frac{\Delta t}{k_B T}\right) \sum_{j=1}^{N} \boldsymbol{D}_{ij} \cdot (\boldsymbol{F}_j{}^{mag} + \boldsymbol{F}_j{}^{bend} + \boldsymbol{F}_j{}^{const}) + N(0, 2Dt), \tag{B7a}$$

$$\Delta x_i = \boldsymbol{r}_{\boldsymbol{i}}(t+\Delta t) - \boldsymbol{r'}_{\boldsymbol{i}}(t+\Delta t) = \left(\frac{\Delta t}{k_B T}\right) \sum_{j=1}^{N} \boldsymbol{D}_{ij} \cdot \left(\boldsymbol{F}_j{}' - \boldsymbol{F}_j{}^{mag} - \boldsymbol{F}_j{}^{bend} - \boldsymbol{F}_j{}^{const}\right), \tag{B7b}$$

where the diffusion constant $D = k_B T / 6\pi\eta a$, and $\boldsymbol{F}_j{}'$ is the forces calculated for the conformation $\boldsymbol{r'}_{\boldsymbol{i}}(t+\Delta t)$ calculated in Eq. (B7a).

REFERENCES

[1] O. Chaudhuri, S. H. Parekh, and D. A. Fletcher, Nature **445**, 295 (2007).
[2] G. Bao and S. Suresh, Nature **2**, 715 (2003).
[3] S. C. Schuster and S. Khan, Annu. Rev. Biophys. Biomol. Struct. **23**, 509 (1994).
[4] E. Lauga and T. R. Powers, Reports Prog. Phys. **72**, 96601 (2009).
[5] L. E. Becker and M. J. Shelley, Phys. Rev. Lett. **87**, 198301 (2001).
[6] S. B. Kharchenko, J. F. Douglas, J. Obrzut, E. A. Grulke, and K. B. Migler, Nat. Mater. **3**, 564 (2004).
[7] L. D. Landau, E. M. Lifshitz, J. B. Sykes, W. H. Reid, and E. H. Dill, *Theory of Elasticity: Vol. 7 of Course of Theoretical Physics* (Butterworth-Heinemann, 1960).
[8] V. Kantsler and R. E. Goldstein, Phys. Rev. Lett. **108**, 038103 (2012).
[9] J. W. Swan, P. A. Vasquez, and E. M. Furst, Phys. Rev. Lett. **113**, 138301 (2014).
[10] A. A. Evans, S. E. Spagnolie, D. Bartolo, and E. Lauga, Soft Matter **9**, 1711 (2013).
[11] L. Li, H. Manikantan, D. Saintillan, and S. E. Spagnolie, J. Fluid Mech **735**, 705 (2017).
[12] A. Cebers and K. Erglis, Adv. Funct. Mater. **26**, 3783 (2016).
[13] R. Dreyfus, J. Baudry, M. L. Roper, M. Fermigier, H. A. Stone, and J. Bibette, Nature **437**, 862 (2005).
[14] M. Roper, R. Dreyfus, J. Baudry, M. Fermigier, J. Bibette, and H. A. Stone, Proc. R. Soc. A Math. Phys. Eng. Sci. **464**, 877 (2008).

[15] S. L. Biswal and A. P. Gast, Anal. Chem. **76**, 6448 (2004).
[16] T. Yang, T. O. Tasci, K. B. Neeves, N. Wu, and D. W. M. Marr, Langmuir **33**, 5932 (2017).
[17] S. Kuei, B. Garza, and S. L. Biswal, Phys. Rreview Fluids **2**, (2017).
[18] J. M. Dempster, P. Vázquez-Montejo, and M. Olvera de la Cruz, Phys. Rev. E **95**, 052606 (2017).
[19] P. Vázquez-Montejo, J. M. Dempster, and M. Olvera De La Cruz, Phys. Rev. Mater. **1**, (2017).
[20] A. Cebers, Curr. Opin. Colloid Interface Sci. **10**, 167 (2005).
[21] C. Goubault, P. Jop, M. Fermigier, J. Baudry, E. Bertrand, and J. Bibette, Phys. Rev. Lett. **91**, (2003).
[22] V. P. Shcherbakov and M. Winklhofer, Phys. Rev. E - Stat. Nonlinear, Soft Matter Phys. **70**, (2004).
[23] M. Roper, R. Dreyfus, J. Baudry, M. Fermigier, J. Bibette, and H. A. Stone, J. Fluid Mech. **554**, 167 (2006).
[24] K. Erglis, D. Zhulenkovs, A. Sharipo, and A. Cebers, J. Physics-Condensed Matter **20**, (2008).
[25] S. Huang, G. Pessot, P. Cremer, R. Weeber, C. Holm, J. Nowak, S. Odenbach, A. M. Menzel, and G. K. Auernhammer, Soft Matter **12**, 228 (2015).
[26] G. Fonnum, C. Johansson, A. Molteberg, S. Mørup, and E. Aksnes, J. Magn. Magn. Mater. **293**, 41 (2005).
[27] J. Byrom, P. Han, M. Savory, and S. L. Biswal, Langmuir **30**, 9045 (2014).
[28] H. Li, T. Shen, D. Vavylonis, and X. Huang, Med. Image Comput. Comput. Assist. Interv. **12**, 673 (2009).
[29] H. Li, T. Shen, M. B. Smith, I. Fujiwara, D. Vavylonis, and X. Huang, Proceedings. IEEE Int. Symp. Biomed. Imaging **2009**, 1302 (2009).
[30] J. Schindelin, I. Arganda-Carreras, E. Frise, V. Kaynig, M. Longair, T. Pietzsch, S. Preibisch, C. Rueden, S. Saalfeld, B. Schmid, J.-Y. Tinevez, D. J. White, V. Hartenstein, K. Eliceiri, P. Tomancak, and A. Cardona, Nat. Methods **9**, 676 (2012).
[31] A. Cebers and I. Javaitis, Phys. Rev. E - Stat. Nonlinear, Soft Matter Phys. **69**, (2004).
[32] R. E. Goldstein and S. A. Langer, Phys. Rev. Lett. **75**, 1094 (1995).
[33] U. Seifert, W. Wintz, and P. Nelson, Phys. Rev. Lett. **77**, 5389(4) (1996).
[34] G. K. Batchelor, J. Fluid Mech. **44**, 419 (1970).
[35] D. Li, N. Fakhri, M. Pasquali, and S. L. Biswal, Phys. Rev. Lett. **106**, 188302 (2011).
[36] C. H. Wiggins, D. Riveline, A. Ott, and R. E. Goldstein, Biophys. J. **74**, 1043 (1998).
[37] O. Hallatschek, E. Frey, and K. Kroy, Phys. Rev. E **75**, (2007).
[38] E. Gauger and H. Stark, Phys. Rev. E **74**, 021907 (2006).
[39] D. J. Griffiths, *Introduction To Electrodynamics 3Rd Ed.* (Prentice-Hall Of India Pvt. Limited, 1999).
[40] K. Kegler, M. Konieczny, G. Dominguez-Espinosa, C. Gutsche, M. Salomo, F. Kremer, and C. N. Likos, Phys. Rev. Lett. **100**, 118302 (2008).
[41] J. Rotne and S. Prager, J. Chem. Phys. **50**, 4831 (1969).
[42] H. Yamakawa, J. Chem. Phys. **53**, 436 (1970).
[43] D. L. Ermak and J. A. McCammon, J. Chem. Phys. **69**, 1352 (1978).
[44] K. Klenin, H. Merlitz, and J. Langowski, Biophys. J. **74**, 780 (1998).
[45] M. Belovs and A. Cebers, Phys. Rev. E **73**, (2006).
[46] O. Hallatschek, E. Frey, and K. Kroy, Phys. Rev. Lett. **94**, 077804 (2005).
[47] O. Hallatschek, E. Frey, and K. Kroy, Phys. Rev. E **75**, (2007).
[48] L. Golubović, D. Moldovan, and A. Peredera, Phys. Rev. Lett. **81**, 3387 (1998).
[49] L. Golubovic, D. Moldovan, and A. Peredera, Phys. Rev. E **61**, 1703 (2000).
[50] A. J. Spakowitz and Z. G. Wang, Phys. Rev. E **64**, 10 (2001).
[51] O. Hallatschek, E. Frey, and K. Kroy, Phys. Rev. E **70**, 19 (2004).
[52] K. S. Turitsyn and S. S. Vergeles, Phys. Rev. Lett. **100**, 028103(4) (2008).
[53] V. Kantsler, E. Segre, and V. Steinberg, Phys. Rev. Lett. **99**, (2007).
[54] K. W. Yung, P. B. Landecker, and D. D. Villani, Magn. Electr. Sep. **9**, 39 (1998).

[55] D. Li, C. N. Lam, and S. L. Biswal, Soft Matter **6**, 239 (2010).
[56] D. Li, S. Banon, and S. L. Biswal, Soft Matter **6**, 4197 (2010).
[57] W. F. van Gunsteren and H. J. C. Berendsen, Mol. Phys. **45**, 637 (1982).